

Journal of Materials Chemistry A

Accepted Manuscript



This is an *Accepted Manuscript*, which has been through the Royal Society of Chemistry peer review process and has been accepted for publication.

Accepted Manuscripts are published online shortly after acceptance, before technical editing, formatting and proof reading. Using this free service, authors can make their results available to the community, in citable form, before we publish the edited article. We will replace this *Accepted Manuscript* with the edited and formatted *Advance Article* as soon as it is available.

You can find more information about *Accepted Manuscripts* in the [Information for Authors](#).

Please note that technical editing may introduce minor changes to the text and/or graphics, which may alter content. The journal's standard [Terms & Conditions](#) and the [Ethical guidelines](#) still apply. In no event shall the Royal Society of Chemistry be held responsible for any errors or omissions in this *Accepted Manuscript* or any consequences arising from the use of any information it contains.

Cite this: DOI: 10.1039/c0xx00000x

Full Papers

www.rsc.org/xxxxxx

Synthesis of hollow organosiliceous spheres for volatile organic compounds removal

Hongning Wang,^a Mei Tang,^a Lu Han,^d Jianyu Cao,^a Zhihui Zhang,^a Weiqiu Huang,^c Ruoyu Chen,^{*a} Chengzhong Yu^{*b}

5 Received (in XXX, XXX) Xth XXXXXXXXX 20XX, Accepted Xth XXXXXXXXX 20XX

DOI: 10.1039/b000000x

Hollow organosiliceous spheres (HOSs) materials have been successfully synthesized by a co-condensation method with tetraethylorthosilicate (TEOS) and organosilane (1,2-bis(triethoxysilyl) ethane, BTSE) as mixed silica sources under acidic conditions. The application of HOSs as adsorbents for the
10 volatile organic compounds (VOCs) abatement was demonstrated. The HOSs were characterized by transmission electron microscopy (TEM), N₂ sorption isotherms, FT-IR spectroscopy techniques, thermogravimetric analyser (TGA) and X-ray photoelectron spectroscopy (XPS). The results indicated that all samples showed a uniform hollow mesostructure and the organic groups were chemically incorporated into the walls of HOSs. The static adsorption and stability behaviors of water vapor, n-
15 hexane and 93# gasoline on HOSs were investigated, with commercial silica gel (SG) and activated carbon (AC) as references. It was found that the sample with an initial molar ratio BTSE/(BTSE+TEOS) of 25% (HOSs-25%) had the largest VOCs adsorption capacity (1.36 g g⁻¹ n-hexane and 1.35 g g⁻¹ 93# gasoline) and smallest water vapor adsorption capacity (0.0120 g g⁻¹) under the static adsorption condition. The dynamic adsorption behaviors of n-hexane on HOSs-25% were evaluated via breakthrough
20 curves. The dynamic adsorption capacities of n-hexane are in the following order: SG < AC < HOSs-25% and the stability is in the order of AC < SG < HOSs-25%. The larger dynamic VOCs capacity of the HOSs may be attributed to the synergetic effect between the unique morphology and hybrid walls. The static and dynamic n-hexane and water vapor competitive adsorption results suggested that HOSs-25% had a much higher adsorption tendency for VOCs over water vapor. The HOSs with high hydrophobicity,
25 large VOCs removal capacity and excellent recyclability show great potential for VOCs controlling.

Keywords: Hollow organosiliceous spheres, n-hexane adsorption, VOCs removal, water vapor adsorption

1. Introduction

The emission of volatile organic compounds (VOCs) is a big
30 issue nowadays because VOCs can cause serious health and environmental problems. Among a number of technologies available for VOCs abatement, physisorption is a reliable method widely used because of the flexibility of the system, low energy and cheap operation costs. 1-3 Activated carbon (AC) is one of the most widespread adsorbents to eliminate VOCs due to its
35 developed microporosity which ensures good adsorption capacities. 4 However, it has been recognized that the AC presents several disadvantages such as fire risk, pore clog, hygroscopicity, and some problems associated with regeneration. 4-6 Hence, different alternative adsorbents are desirable to be
40 developed for VOCs treatment with improved performance.

Mesoporous silicas with large surface areas and high pore

volumes have attracted a great deal of attention due to their wide range of applications in adsorption, catalysis, sensors, and electrical/optical devices. 7 Mesoporous silicas also have great
45 potential for the removal of VOCs because of their large BET surface area, controllable and uniform pore size, open pore structure, high porosity, good mechanical stability, and in particular, reliable desorption performance. 8 The large pores are beneficial for the adsorption of bulky molecules compared to AC
50 materials with dominant micropores. In previous studies, MCM-41, MCM-48, SBA-15 and HMS type mesoporous silicas have been used as adsorbents for the VOCs removal, 2, 9-16 all with pure silica composition in the skeleton. However, the amount of VOCs adsorbed on silica-based mesoporous materials could be
55 significantly reduced in the presence of water vapor because of the strong interaction between water molecules and silanols. 17, 18 Therefore, increasing the hydrophobicity of mesoporous materials is required in order to improve their VOCs adsorption

performance.

One important approach to improve the hydrophobicity of mesoporous materials is through surface organic functionalization.¹⁹ Surface functionalization can be conducted in mainly three ways including surface functionalization of as-synthesized silica materials (“post-synthesis”), simultaneous condensation of silica and organosilica precursors (“co-condensation”), and the incorporation of organic groups as bridging components into the pore walls (“production of periodic mesoporous organosilica”).²⁰ Compared to the post-synthesis grafting procedure, the co-condensation route or the use of bridged organosilica precursors offers advantages including the introduction of homogenous hybrid framework within the pore walls and relatively simple preparation procedures. In previous studies, it has been shown that mesoporous silicas after surface or frame-work functionalization with organic groups possess improved adsorption capacities and selectivity toward hydrophobic substances.^{14, 23, 24} However, the real application of functionalized mesoporous materials in VOCs removal such as in gasoline vapor control has been rarely reported.

Mesoporous hollow siliceous spheres (HSSs) with a large fraction of voids in the interior have attracted considerable interest in the past few decades due to their well-defined hollow structure, high pore volume, thermal and mechanical stability, low density, and biocompatibility.²⁵⁻³² In our previous report, surfactant free HSSs were functionalized by trimethylchlorosilane (TMCS), and the resultant HSSs-TMCS showed high capacity of adsorbing VOCs with good stability and low water vapor adsorption capacity under static adsorption conditions, and high dynamic adsorption capacity and stable breakthrough time under dynamic adsorption conditions.³³ For HSSs-TMCS, the hydrophobic modification occurs only on the surface. It is hypothesized that hollow organosiliceous spheres (HOSs) with hydrophobic groups distributed inside the walls would show a more hydrophobic nature and thus provide a better performance for removing the VOCs from gas stream while simultaneously decreasing the water vapor adsorption capacity.

This study focuses on the synthesis of HOSs using a co-condensation method. HOSs with adjustable molar ratios of organosilane/(organosilane+TEOS) were prepared and used as adsorbents for VOCs abatement. Their static water vapor, n-hexane, 93# gasoline adsorption capacity and stability were evaluated. The dynamic adsorption behaviors of n-hexane were investigated on HOSs with the optimum static adsorption behaviors compared with commercial AC and silica gel (SG). Our results showed that compared to HSSs-TMCS, HOSs possessed decreased water vapor adsorption and much higher VOCs adsorption capacities.

2. Experimental methods

2.1 Materials

Tetraethylorthosilicate (TEOS), hydrochloric acid (HCl), sodium hydroxide (NaOH), sodium chloride (NaCl), n-hexane, toluene, and ethanol were purchased from Shanghai Chemical Crop. 1,2-bis(triethoxysilyl) ethane (96%) (BTSE), Pluronic F108 (EO₁₃₂PO₆₀EO₁₃₂, where EO is polyethylene oxide and PO is polypropylene oxide, Mw=14600) were purchased from Sigma-

Aldrich. 1,3,5-trimethylbenzene (TMB) and dimethoxydimethylsilane (DMDMOS) were purchased from Aladdin Chemistry Company. 93# gasoline was purchased from Sinopec. All chemicals were used as received without further purification.

2.2 Synthesis

A series of HOSs were prepared by adjusting the ratio of TEOS and BTSE. The samples are named as HOSs- ϕ , where ϕ is molar ratio of BTSE/(BTSE+TEOS) in the initial synthesis system (ϕ varied between 5% and 30%, and the total mole of BTSE and TEOS was kept at 4.81×10^{-3}). In a typically synthesis, 1.0 g of F108 was dissolved in 30 g of 2.0 M HCl, then 1.0 g of TMB was added into the solution and stirred vigorously for 6 h at 25 °C. Then, 0.42 g of BTSE and 0.75 g of TEOS ($\phi=0.25$) were added dropwise to the surfactant solution under vigorous stirring. After stirring for 6 h, 0.50 g of DMDMOS was introduced into the system and the reaction was continued for 24 h. The resulting solution was transferred into 100 mL stainless, Teflon-lined autoclave and heated at 100 °C for 24 h. The milky mixture was dialyzed in deionized water for 48 h using a semi-permeable membrane (molecular-weight cutoff of 14000). White powders were obtained by evaporation of the solution after dialysis. The solid products were collected and then extracted with 100 mL of ethanol (99.0%) and 2 mL of HCl (37 wt%) at 80 °C for 12 h to remove the F108 template. The final HOSs products were collected after filtration, ethanol washed and dried in 80 °C oven. The sample was named as HOSs-25%.

2.3 Sample characterization

Transmission electron microscopy (TEM) experiments were conducted on a JEOL2011 microscope (Japan) operated at 200 kV. The samples for TEM measurements were suspended in ethanol and supported onto a holey carbon film on a Cu grid. Nitrogen sorption isotherms were measured at 77 K with a Micromeritics ASAP 2020 analyzer. The high pressure N₂ adsorption capacity was investigated (at 273 and 298 K) using a high pressure volumetric analyzer (H-Sorb 2600). The pressure of N₂ was increased in a stepwise manner from 0 to 10 bar. Before measurements, the samples were degassed in a vacuum at 150 °C for at least 12 h. The Brunauer-Emmett-Teller (BET) method was utilized to calculate the specific surface areas (S_{BET}) using adsorption data in a relative pressure range from 0.05 to 0.30. The pore size distributions and pore volume were derived from the adsorption branches of the isotherms. By using the Barrett-Joyner-Halenda (BJH) model, the pore size distributions were derived. The total pore volumes (V_t) were calculated from the nitrogen amount adsorbed at a relative pressure of 0.98. The micropore volumes (V_m) and micropore surface areas (S_m) were calculated from the t-plot method.³⁴ The isosteric heats of adsorption (Q_{st}) for N₂ are calculated by using the Clausius-Clapeyron equation.^{35, 36} Fourier transform infrared (FT-IR) spectra were collected on Nicolet Fourier spectrophotometer, using KBr pellets of the solid samples. The thermogravimetry (TG) analyses of different HOSs were performed on TG/DTA analyser (EXSTAR6000). The heating rate was 10 °C min⁻¹ from 35 °C to 900 °C under an air flow of

20 mL min⁻¹. XPS analysis was performed on a PHI 5000 Versaprobe system, using monochromatic Al K α radiation (1486.6 eV). All binding energies (BE) were referenced to the C1s peak at 284.5 eV.

5 2.4 Static isotherm adsorption measurements

Static adsorption equilibrium measurements at room temperature were carried out using a digital microbalance (Model YP/1002) with a sensitivity of 0.1 mg.³⁷ The adsorption-desorption properties of the VOCs or water vapor were determined in a desiccator with a series of VOCs or distilled water under the plate at the respective saturation pressure (water vapor of 3.17 kPa, n-hexane of 20.00 kPa, and 93# gasoline of 41.50 kPa, respectively). The desiccator was placed in a constant-temperature water container and equipped with an analytical balance. First, the powder sample was loaded on a weighting bottle (50 mm x 30 mm) without lid. Under a high-vacuum of 0.9 mbar, the sample was heated to 100 °C for at least 2 h to remove all adsorbed impurities. After that, the weighting bottle (with lid) was cooled to the room temperature in drying apparatus. Then the weighing bottle (without lid) with adsorbent inside keep in contact with the VOCs or water vapor for sufficient time at 25 °C. After the adsorption became saturated, the desorption procedure was carrying out by heating the sample to 100 °C in a vacuum environment for 75 min (until the mass of the sample do not change any more). All the static adsorption experiments were performed in triplicate (each including 5 adsorption-desorption cycles) to ensure the reproducibility of the data. According to the mass change of the sample before and after the adsorption and desorption procedure, the adsorption capacity and desorption percentage of the sample could be calculated as follows:

$$X = \frac{m_2 - m_1}{m_1} \quad (1)$$

$$Y = \frac{m_3 - m_4}{m_2 - m_1} \times 100\% \quad (2)$$

Where X and Y are the adsorption and desorption rate of the sample, m_1 and m_2 are the mass of the sample before and after the adsorption, m_3 and m_4 are the mass of the sample before and after the desorption, respectively.

For clarification of water vapor on n-hexane static sorption performance for HOSs-25%, control experiments with 4:1 and 1:1 (volume ratio) n-hexane and water mixture as adsorbates were performed. Meanwhile, the cycling performance was also done under the same conditions. After 24 h static adsorption at room temperature, the adsorbents were transferred into 250 mL iodine flask with ethanol as the extractant (1g adsorbent/250 mL ethanol) immediately. Then the iodine flask was put in constant temperature oscillator with shaking at 200 r min⁻¹ at room temperature for 5 h. The adsorbed amount of n-hexane of static competitive of n-hexane and water experiment (m_{hexane}) was determined by the concentration tested using a gas chromatograph (GC) equipped with a flame ionization detector. The total static n-hexane and water vapor adsorption amount (m_t) was calculated according to the mass change of the sample before and after the adsorption. The static water vapor adsorption amount (m_{water}) was the difference value of m_t and m_{hexane} . The corresponding adsorption capacity and desorption percentage

calculations of the sample were similar to that of static single component adsorption.

2.5 Titration of surface hydroxyl

The density of surface hydroxyl was determined according to Boehm titration.^{33, 38, 39} Typically, 0.50 g of sample was dispersed in 100 mL mixture of ethanol and NaCl and then sealed and shaken thoroughly for 24 h. The pH value of the resulting suspension was first adjusted to 4.0 by 0.01 M HCl or 0.018 M NaOH and then the pH was further titrated from 4.0 to 9.0 with 0.018 M NaOH. The density of surface hydroxyl was calculated as follow:

$$D = C \cdot V \cdot N_A \times 10^{-3} \quad (3)$$

which D ($\times 10^{20}$ g⁻¹) was the density of surface hydroxyl of the sample, C, V and N_A were the concentration of NaOH (M), which was calibrated by C₈H₅KO₄, the titration volume of NaOH (mL) during the pH value of the resulting suspension varied from 4.0 to 9.0 and the Avogadro constant, respectively.

2.6 Dynamic adsorption measurements

The dynamic adsorption was carried out by a flow method reported by Hu et al.⁴⁰ About 3.0 g of sample was loaded in a fixed-bed reactor. Before adsorption measurements, samples were degassed at 100 °C overnight under vacuum condition to remove the physically adsorbed water molecules and small organic impurities. Air was taken as a carrier gas and adjusted to keep a total flow rate of 0.135 L min⁻¹ (with n-hexane concentration of 800 000 ppm).¹⁴ The adsorbed amount of adsorbate was determined by the concentration change before and after adsorption measurements tested by using a GC equipped with a flame ionization detector. The equilibrium dynamic adsorption capacity (q) of the adsorbents was calculated from the breakthrough curves according to the equation as follows:

$$q = \frac{F_A \int (1 - \frac{C_A}{C_0}) dt}{W} \quad (4)$$

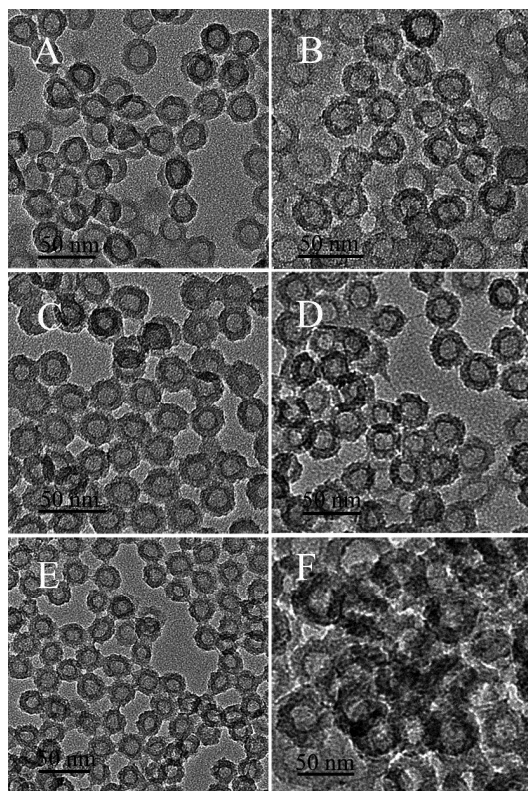
Where C_A and C_0 were the outlet and inlet concentrations (g L⁻¹) of the stream through the fixed bed column, respectively. F_A (L min⁻¹) was the mixed gas flow rate of n-hexane and air, and W (g) was the amount of the adsorbent loaded in the adsorption bed. The time rang of integration was from 0 to t_e (min), where t_e was adsorption equilibrium time. For clarification of water vapor on n-hexane dynamic sorption performance for HOSs-25%, control experiments using water-saturated carrier gas were performed. Meanwhile, the cycling performance was also done under the same conditions. The n-hexane equilibrium dynamic adsorption capacity (q_{hexane}) was calculated from the breakthrough curves according to equation (4). The total equilibrium dynamic adsorption capacity (q_t) was calculated according to the mass change of the sample before and after the dynamic adsorption by using equation (1) and the calculation of desorption percentage for the sample was similar to that of static adsorption process. The water vapor equilibrium dynamic adsorption capacity (q_{water})

was calculated by $q_t - q_{\text{hexane}}$.

3. Results and discussion

3.1 Characterization of samples

5 TEM images of HOSs ($\phi=5\%-30\%$) after extraction with acidic ethanol solutions are shown in Fig.1. All the HOSs samples show well dispersed spheres except HOSs-30% showing a highly aggregated nature. The particle sizes of HOSs ($\phi=5\%-25\%$) measured from TEM measurements are in the range of 23-28 nm. 10 With an increase of ϕ , the pore diameters of the HOSs measured also from TEM decrease, while the particle sizes and wall thicknesses increase at first, and decrease with ϕ further increase (Fig.S1). When ϕ increases to 25%, uniform hollow spheres are also observed, and particle size of the hollow mesopores is about 15 23 nm (Fig.1E). These results clearly demonstrate that uniform and well dispersed HOSs with large cavities can be obtained in the range of $\phi=5\%-25\%$. When ϕ was further increased to 30%, the obvious aggregation of spheres can be observed (Fig.1 F). Under acidic conditions, the hydrolysis and condensation of 20 BTSE is much faster compared to that of TEOS. The interparticle cross-linking or the condensation of BTSE itself may cause the aggregation of products when ϕ is higher than 30%.



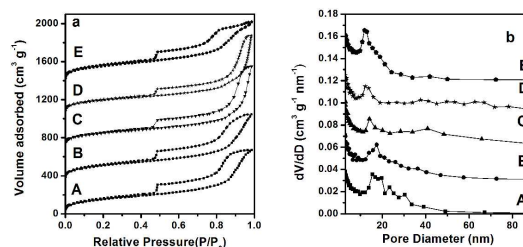
25 **Fig. 1** TEM images HOSs-5% (A), HOSs-10% (B), HOSs-15% (C), HOSs-20% (D), HOSs-25% (E), and HOSs-30% (F), respectively.

For comparison, the extracted HOSs-5% and HOSs-25% were synthesized under exactly the same conditions but without 30 introducing DMDMOS. The obtained spheres are hollow and uniform, but the aggregation is obvious (as shown in Fig.S2). For

the synthesis of HOSs, the highest ϕ to maintain the dispersed morphology is 25%, thus a large portion of pure silica is present in the wall matrix. The abundant silanol groups on the outer 35 surface of each particle are the main reason for the inter-particle aggregation due to further cross-linking. The role of DMDMOS is to form a hydrocarbon chain terminated outer surface, minimizing the aggregation of HOSs during the co-condensation process.^{31, 41, 42}

40 The textural properties of the organic-inorganic hybrid hollow spheres were analyzed by N_2 adsorption-desorption isotherms (Fig.2). The HOSs show typical type IV isotherms of mesoporous materials (Fig.2a). It is noteworthy that there are two capillary condensation steps in the adsorption isotherms, suggesting that 45 the samples have two types of mesopores. The primary pore can be ascribed to the inner void of the hollow nanospheres, and the secondary mesopore corresponds to the interparticle void formed from the packing of the nanospheres.^{31, 43-47} As also shown in Fig.2a, a small position shift of the capillary condensation toward 50 lower relative pressures can be observed with the increase of ϕ , which indicates the decrease of the mesopore size⁴⁸ as can be confirmed by Fig.2b, and is consistent with the TEM observation (Fig. 1 and Fig. S1). The physicochemical properties of HOSs with different ϕ are listed in Table 1. The BET surface areas and 55 pore volumes show no clear tendency as ϕ increases.

The change of pore diameters as a function of ϕ can be explained by the co-condensation protocol used to prepare HOSs. The particle sizes are measured to be varied in a small range of 23-28 nm for all particles. In our synthesis, F108 is used as the 60 surfactant, which contains both hydrophilic PEO and hydrophobic (PPO) segments.³⁰ TEOS and BTSE are used as mixed precursors with BTSE being more hydrophobic. The formation of the hollow morphology follows a hard sphere templating mechanism (Hard-sphere packing and icosahedral 65 assembly in the formation of mesoporous materials.).³⁰ TEOS after hydrolysis is most likely incorporated in the PEO region, while BTSE penetrates deeper into the hydrophobic cores due to its hydrophobic nature.⁴⁹ The hydrolysis and condensation of BTSE in the hydrophobic domain leads to the decrease of pore 70 size. Consequently, with increasing molar ratio of BTSE (ϕ), the pore diameter further decreases.



75 **Fig. 2** N_2 adsorption-desorption isotherms (a) and pore size distributions (b) for HOSs-5% (A), HOSs-10% (B), HOSs-15% (C), HOSs-20% (D), and HOSs-25% (E), respectively. The Y-axes value of HOSs-10%, HOSs-15%, HOSs-20%, and HOSs-25% in (a) is raised 350, 700, 1050, and 1400 $\text{cm}^3 \text{g}^{-1}$, respectively. In (b), the Y-axes value is 0.03, 0.06, 0.09 and 0.12 $\text{cm}^3 \text{g}^{-1}$ higher for HOSs-10%, HOSs-15%, HOSs-20%, and 80 HOSs-25%, respectively.

Table 1. Structural parameters of different HOSs samples.

Samples	S_{BET} ($\text{m}^2 \text{g}^{-1}$)	S_{m} ($\text{m}^2 \text{g}^{-1}$)	V_{t} ($\text{cm}^3 \text{g}^{-1}$)	V_{m} ($\text{cm}^3 \text{g}^{-1}$)
HOSs-5%	548	145	1.03	0.06
HOSs-10%	572	167	1.04	0.07
HOSs-15%	539	169	1.31	0.07
HOSs-20%	518	158	1.16	0.07
HOSs-25%	572	138	0.92	0.06

The incorporation of organic groups in the HOSs frameworks can be qualitatively confirmed by the FT-IR spectra in Fig.3. The intensity of the peaks at 1460 cm^{-1} and $2850\text{--}3000 \text{ cm}^{-1}$ due to the F108 surfactant residues is very weak (Fig.3), suggesting the relatively effective removal of the surfactant by the solvent extraction method. The band at 2974 cm^{-1} is assigned to the C-H bond stretching vibration of the terminal methyl group. The FT-IR spectra of all the HOSs (Fig.3A-E) show one intense band at 1272 cm^{-1} , which can be attributed to the Si-C bond. The intensities of C-H bond and Si-C bond increased with more BTSE introduced into the HOSs. The spectra contain a broad band at $\sim 3500 \text{ cm}^{-1}$, related to the silanol groups interacting by the hydrogen bonds. The absence of the band at 3750 cm^{-1} , which should be attributed to the isolated terminal silanols, indicated that most of the isolated terminal silanols had been incorporated with BTSE. The peak at 1634 cm^{-1} can be attributed to the O-H bending vibration mode of the adsorbed water molecules, which showed small intensity, indicating little hydroxyl which was favorite for VOCs adsorption. The intensity of silanol groups and O-H bending vibration mode of the adsorbed water molecules were decreased with more BTSE introduced, of which HOSs-25% was the weakest, and which was much weaker as compared to that of SG.

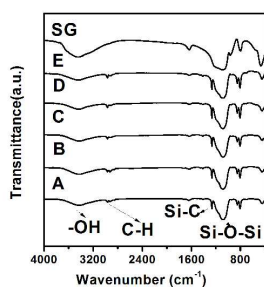


Fig. 3 FT-IR pattern of HOSs-5% (A), HOSs-10% (B), HOSs-15% (C), HOSs-20% (D), HOSs-25% (E) and SG, respectively.

C1s XPS plots of HSSs and HOSs was shown in Fig. S3. The fitting of C1s emission revealed two different environments of the C-atoms. The peak at about 284.8 eV corresponds to either C-C or C-H bonds, while the peak at about 284.0 eV corresponds to either C-Si bonds. Compared with HSSs, the obvious increase of C-Si bonds for HOSs-5% and HOSs-25% together with the increasing of Si and C atomic ratios (Table S1) suggests the successful incorporation of BTSE, agreeing well with the FT-IR results.

The thermal stability of the incorporated functional groups was studied by using TGA technique (Fig. S4). It can be seen that all HOSs exhibit multistep weight loss due to loss of different species. The small amount of weight loss (below 1%) at $100 \text{ }^\circ\text{C}$

was caused by the loss of physisorbed water. The weight loss (11-16%) at temperatures between 250 and $800 \text{ }^\circ\text{C}$ is mainly associated with the loss of organic fragments coming from both BTSE and DMDMOS precursors in the pore walls. Meanwhile, the condensation of Si-OH may generate water molecules, therefore it is difficult to distinguish the amount of weight loss coming from BTSE. However, the organic content in all samples either measured by TGA or calculated from the feeding ratio has no significant difference for all HOSs (Table S2). This is because in our synthesis, the amount of DMDMOS is fixed (46.4%, molar ratio) while BTSE contributes only a small fraction in the organo groups in the wall framework (2.68%-13.4%, molar ratio)

3.2 Static adsorption

3.2.1 Water vapor adsorption-desorption behaviour

Water vapor is often present at high levels in gas streams. Many studies have pointed out that water vapor can compete with VOCs and thus influence the adsorption process, resulting in a diminished capacity and a slow adsorption kinetics for the targeted adsorbates, especially at high relative humidity. Although mesoporous silica have larger pores and high surface area which make them accessible to bulky molecules, their hydrophilic feature due to a large number of silanols (Si-OH) on their amorphous wall surfaces still affects their ability for the removal of VOCs. Therefore it's very important to study the water vapor adsorption-desorption capacity. The static adsorption-desorption capacity of water vapor on all the samples was based on the mass change of the samples before and after the adsorption or desorption procedure. The histograms of water vapor adsorption capacity on different HOSs samples are presented in Fig.4a. The corresponding histograms of commercial samples (AC and SG) are also presented (Table 2 and Fig. 4b) for comparison. The water vapor desorption capacities of different materials are listed in Table 2. To understand the difference in the water vapor adsorption performance of various materials, the surface hydroxyl density was titrated and the results are summarized in Table 2.

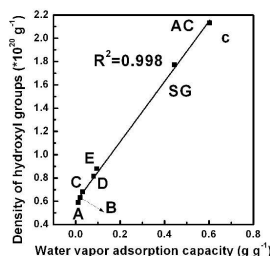
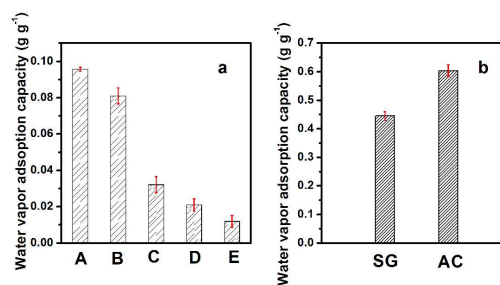


Fig. 4 The histograms of static water vapor adsorption capacity from triplicate measurements on different HOSs (a), SG and AC (b), and the relationship between static water vapor adsorption capacity and the density of surface hydroxyl group (c). A-E is HOSs-5% (A), HOSs-10% (B), HOSs-15% (C), HOSs-20% (D) and HOSs-25% (E), respectively.

In Table 2, it is evident that the water vapor adsorption capacity of different materials under study is proportional to the density of surface hydroxyl. HOSs-5% exhibits the highest water vapor adsorption capacity (0.0957 g g^{-1}) among different HOSs samples, owing to the high density of surface hydroxyl ($0.879 \times 10^{20} \text{ g}^{-1}$), but smaller than that of HSSs-ex (0.118 g g^{-1}).³³ With increasing amounts of ethane groups in the framework, water vapor adsorption capacity was found to be decreased and comparable to the incorporated BTSE content in the materials, at the same time, the density of surface hydroxyl also decreased, correspondingly. HOSs-25% sample has the lowest water adsorption capacity (0.0120 g g^{-1}) and the smallest surface hydroxyl density ($0.588 \times 10^{20} \text{ g}^{-1}$) among all the HOSs samples, which is lower than that of HSSs-TMCS (0.0337 g g^{-1}).³³ This result is in accordance with the FT-IR observation on the decreased peak intensities of Si-OH and adsorbed water molecules groups (Fig. 3). Such a decrease in water vapor adsorption capacity is due to the increase in hydrophobic character of the materials upon incorporation of bridging ethane groups in the mesoporous network and the decrease of the accessible silanol groups. In addition, the water vapor adsorption capacity of different HOSs are far lower than that of SG (0.445 g g^{-1}) and AC (0.604 g g^{-1}), which may be due to the much more surface hydroxyl groups of commercial adsorbents (1.77 and $2.13 \times 10^{20} \text{ g}^{-1}$, respectively, Table 2). Fig. 4c depicts the relationships between the density of surface hydroxyl groups and the water vapor adsorption capacities for different samples. The relationship between water vapor adsorption capacities of all the samples and the corresponding densities of surface hydroxyl groups is linear, where the linear fitting coefficient $R^2 = 0.998$ (as shown in the Fig. 4c), which reveals that the amount of adsorbed water molecules on the adsorbents is greatly influenced by the accessible silanol groups. As can also be seen in Fig. S5, the density of surface hydroxyl groups are irrelevant to the corresponding structural parameters. And the introduction of BTSE into the framework can decrease the density of accessible surface hydroxyl groups and is favourable for minimizing water vapor adsorption.

Table 2. The water vapor adsorption capacities, desorption efficiencies and the densities of surface hydroxyl group of different samples.

Samples	Adsorption		Desorption		-OH ^b / $\times 10^{20} \text{ g}^{-1}$
	Average ge(g g^{-1}) 1)	STDE a(%)	Average (%)	STDE ^a (%)	
HOSs-5%	0.0957	0.11	99.7	0.65	0.879
HOSs-10%	0.0810	0.44	99.8	0.76	0.814
HOSs-15%	0.0321	0.45	99.4	0.48	0.681

HOSs-20%	0.0210	0.34	99.6	0.97	0.630
HOSs-25%	0.0120	0.33	99.2	0.34	0.588
SG	0.445	1.50	97.6	0.73	1.77
AC	0.604	2.10	98.1	0.61	2.13

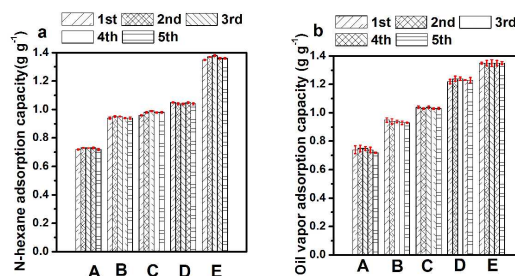
Note: Due to the mass loss of the sample, the percentage of desorption might be higher than 100%, the same below.

^aSTDE refers to standard deviation.

^bThe density of surface hydroxyl groups was determined by Boehm titration method.^{33, 38, 39}

3.2.2 VOCs adsorption-desorption capacity

N-hexane has been used as the representative of VOCs to evaluate the static adsorption capacity of different HOSs materials. The adsorption capacity of n-hexane and 93# gasoline on different HOSs samples are also shown in Fig. 5. As shown in Fig.5a, the static n-hexane adsorption capacity of HOSs-5% is 0.732 g g^{-1} . With more BTSE was introduced, the n-hexane adsorption capacity is increased, and HOSs-25% sample has the largest n-hexane adsorption capacity (1.36 g g^{-1}) (Fig. 5a and Table S3), which is almost two times of that of HSSs-TMCS.³³ It is noted that the adsorption capacities of 93# gasoline on different HOSs samples show the same trend to that of n-hexane (Fig.5b). HOSs-5% and HOSs-25% have the lowest and highest 93# gasoline adsorption capacity, and the corresponding results are 0.740 g g^{-1} and 1.35 g g^{-1} , respectively. These results are consistent with the water adsorption experiments: for HOSs materials with similar structures, a reduction in hydrophilic surface hydroxyl groups by co-condensation of BTSE with hydrophobic functional groups and TEOS favors VOC adsorption and minimizes water adsorption. The adsorption capacity of n-hexane and 93# gasoline on commercial samples AC and SG are also shown in Fig. 5. The n-hexane and 93# gasoline adsorption capacity of SG in the first cycle are 0.438 g g^{-1} and 0.445 g g^{-1} (Fig.5c and d), respectively, and the adsorption capacities are stable. As to the adsorption capacity of AC, in the first cycle n-hexane and 93# gasoline adsorption capacity are 0.639 g g^{-1} and 0.666 g g^{-1} (Fig. 5c and d), respectively. However, the n-hexane and 93# gasoline adsorption capacity decreased in the second cycle, then changed slightly in the third cycle, and then kept constant during the following adsorption process.



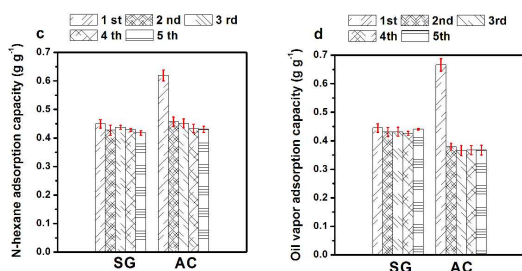


Fig. 5 The histograms of static adsorption capacity from triplicate measurements of different HOSs, n-hexane (a), 93# gasoline (b), and the histograms of static adsorption capacity of AC and SG, n-hexane (c), 93# gasoline (d), respectively. A-E is HOSs-5%, HOSs-10%, HOSs-15%, HOSs-20% and HOSs-25%, respectively.

Fig. S6 depicts the relationships between the densities of surface hydroxyl groups and the static VOCs adsorption capacities for different samples. As can be seen from Fig. S6a and b, the static n-hexane and 93# gasoline adsorption capacities are not related to the corresponding densities of surface hydroxyl groups. The relationships between the static n-hexane adsorption capacities and the corresponding structure parameters of different adsorbents are shown in Fig. S7. The static n-hexane adsorption capacities of different HOSs are irrelevant to the respective micro surface areas, micro pore volumes and surface areas (Fig. S7a-c). As can be seen in Fig. S7d, a higher pore volume directly leads to an increase in the adsorption capacities for n-hexane from HOSs-5% ($1.03 \text{ cm}^3 \text{ g}^{-1}$ and 0.732 g g^{-1}) to HOSs-15% ($1.36 \text{ cm}^3 \text{ g}^{-1}$ and 0.978 g g^{-1}) (Table 1 and Fig. 5a) and is therefore an essential factor in determining the adsorption capacity of adsorbents. However, it must be noted that the VOC adsorption capacities are also associated with the composition of the HOSs. Because with the introduced BTSE was further increased to 20% and 25%, the pore volumes of HOSs-20% ($1.16 \text{ cm}^3 \text{ g}^{-1}$) and HOSs-25% ($0.92 \text{ cm}^3 \text{ g}^{-1}$) decreased (Table 1), but the corresponding n-hexane adsorption capacities were much higher (1.05 g g^{-1} and 1.36 g g^{-1} , respectively) (Fig. S7d). So the VOC adsorption capacity of HOSs may be due to the synergetic effect of the structure and the composition. The competitive adsorption capacities of n-hexane and water vapor for HOSs-25% are shown in Fig. S8. With the volume ratio of n-hexane changed from 4:1 to 1:1, the n-hexane adsorption capacity decreased from 1.34 g g^{-1} to 1.27 g g^{-1} , a little lower than that of single component adsorption (1.36 g g^{-1}). At the same time, the corresponding water vapor capacity increased from 0.0128 g g^{-1} to 0.0148 g g^{-1} . The results suggested that HOSs-25% has a much higher adsorption tendency for n-hexane over water.

The desorption behavior of the adsorbents is very important for their reuse. It would be ideal for practical applications if VOCs can be recovered using mild heat treatment and simultaneously the adsorbents can be regenerated. From the measurement of the desorption capacity of all HOSs samples, a nearly complete desorption of water vapor (Table 2), n-hexane and 93# gasoline can be found (Fig. S9a and b). As shown in Fig. S9c and d, SG has stable and high n-hexane and 93# gasoline desorption efficiencies (almost 100%). As to AC, the desorption efficiencies are low (73.2% for n-hexane and 57.3% for 93# gasoline,

respectively) during the first desorption process, and the desorption efficiencies can reach 100% during the second and the following desorption process.

In order to evaluate the strength of adsorbate/adsorbent interactions, equilibrium data for N_2 onto HOSs-25% and SG were obtained at 273 K and 298 K at pressure up to 10 bar. The N_2 equilibrium isotherms and the calculated isosteric adsorption heats were presented in Fig. S10. An increase in temperature diminishes the amount of N_2 adsorbed of SG and HOSs-25% (Fig. S10a and b). Likewise, the adsorption capacity decreases with decreasing pressure. The shape of the N_2 adsorption isotherms is nearly linear, and the amount of N_2 adsorbed increases linearly with pressure. As shown in Fig. S10c and d, isosteric adsorption heats with respect to N_2 for SG and HOSs-25% are $20\text{--}22 \text{ kJ mol}^{-1}$ and $7\text{--}9 \text{ kJ mol}^{-1}$, respectively. The isosteric adsorption heat of HOSs-25% is lower than that of the reported adsorbents, e.g., MOFs ($12\text{--}15 \text{ kJ mol}^{-1}$),^{60,61} COFs (20.3 kJ mol^{-1}),³⁶ ZIFs ($11\text{--}13 \text{ kJ mol}^{-1}$),^{62,63} and ACs ($14\text{--}16 \text{ kJ mol}^{-1}$),^{64–66} respectively, which means that the interaction between N_2 and HOSs-25% is smaller than that of SG and the reported MOFs, COFs, ZIFs and ACs. The remarkable and stable adsorption capacity of n-hexane and 93# gasoline, a high adsorption tendency for n-hexane over water vapor, along with the complete desorption capacity indicate that the HOSs samples are excellent adsorbents for VOCs removal.

3.3 Dynamic adsorption-desorption behaviour

In many practical VOCs adsorption processes, a fixed bed packed by the adsorbents is used. From the above studies, HOSs-25% with the highest VOCs adsorption capacity, stability, and the lowest water vapor adsorption capacity was adopted to investigate the dynamic adsorption and desorption performance by comparing with AC and SG. To determine the dynamic adsorption performance of adsorbents, the breakthrough time, equilibrium adsorption capacity, and stability are important parameters. Generally, longer breakthrough time results in higher dynamic adsorption capacity.⁴⁰ The equilibrium adsorption capacity was obtained by measuring the area between the maximum baseline and experimental curves. The breakthrough curves of HOSs-25%, SG and AC are shown in Fig. 6 and the corresponding dynamic adsorption results are listed in Table 3.

In Fig. 6, it is obvious that HOSs-25% represents the longest breakthrough time of n-hexane (59 min) during the first dynamic adsorption process and AC is the second one (38 min). SG exhibits shortest breakthrough time (16 min) for n-hexane, which can be attributed to the low surface areas and pore volumes³³ (Fig.S11 and Table S4). The dynamic equilibrium adsorption capacities of n-hexane increase in the order of $\text{SG} (0.367 \text{ g g}^{-1}) < \text{AC} (0.574 \text{ g g}^{-1}) < \text{HOSs-25%} (1.34 \text{ g g}^{-1})$ (Table 3). However, the post-breakthrough curves of AC for n-hexane adsorption increase more gradually with time compared with the other two samples, implying significantly large mass transfer resistance in AC under experimental conditions.¹⁶ In contrast, the post-breakthrough sharpness of the increase in n-hexane concentration for HOSs-25% and SG is more rapid, implying less diffusion resistance in the adsorbents during the adsorption process and fast mass transport, effective adhesion to substrates.⁶⁷ The dynamic adsorption results indicate that the HOSs exhibit an excellent

adsorption performance with higher dynamic adsorption capacity than SG and less mass transfer resistance than AC. The high adsorption capacity for n-hexane could be attributed to the hydrophobicity of the ethane groups embedded inside the silica walls, which improves the affinity for n-hexane to a larger extent.

To test the reusability, the HOSs-25%, SG and AC were regenerated under the same conditions by heating the samples to 100 °C in a vacuum environment for 75 min, and the regenerated adsorbents were subjected to adsorption-desorption cycles at least 8 cycles to observe the change of breakthrough time and equilibrium adsorption capacity. As shown in 6c and d, SG and HOSs-25% have stable breakthrough time and dynamic equilibrium adsorption capacity in at least 8 cycles with very slight variations. As for AC, the breakthrough time and the dynamic equilibrium adsorption capacity decreased dramatically in the second cycle, then changed slightly in the third cycle and the following process, similar to that observed in the static adsorption process. The N₂ sorption results of AC after the 8th adsorption-desorption cycle show that the surface area and pore volume decreased distinctly (Fig. S11 and Table S4), indicating degeneration of AC.⁶⁸

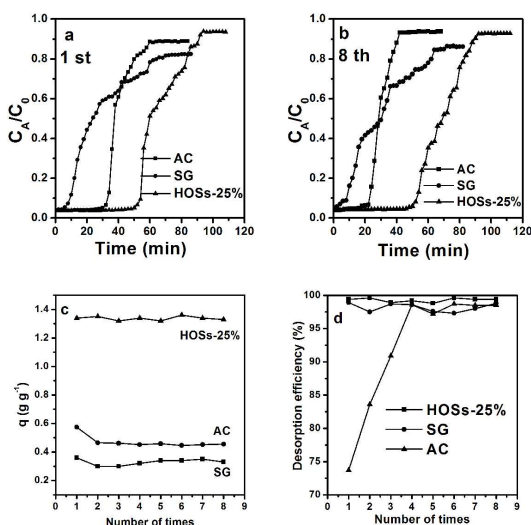


Fig. 6 The breakthrough curves for n-hexane of SG (■), AC (●) and HOSs-25% (▲). (a) is the first time, (b) is the eighth time, (c) and (d) are the comparison of the equilibrium adsorption capacities and desorption efficiencies of eight times, respectively.

Table 3. Comparison of dynamic adsorption parameters of n-hexane on different samples between the first and the eighth time.

Samples	Breakthrough time (min)	t_c (min)	q (g g ⁻¹ adsorbent)	Desorption efficiency (%)
HOSs-25%-1st	59	96	1.34	99.4
SG-1st	16	72	0.367	98.9
AC-1st	38	50	0.574	73.7
HOSs-25%-8th	55	92	1.33	99.4

SG-8th	10	72	0.329	98.8
AC-8th	24	42	0.455	98.5

The first desorption efficiency of HOSs-25%, SG, and AC were 99.4%, 98.9%, and 73.7%, respectively (Table 3). The n-hexane molecules weakly adsorbed on the external surface or the open mesopores of HOSs-25% and SG adsorbents can be easily desorbed by vacuum. However, the desorption efficiency for AC in the first cycle is only 73.7%, and the breakthrough time and the equilibrium adsorption capacity decreased dramatically in the second cycle (Fig. 6c and d), similar to that observed in the static adsorption process. It is suggested that AC has rich micropores, thus the adsorbed hydrocarbons with large molecular weights in the micropores cannot be easily desorbed efficiently under mild conditions.⁶⁸ It may be due to that the n-hexane adsorbed in the micropores of AC is strongly held by adsorption forces and the strongly adsorbed molecules can resist the effects under vacuum. As can be seen in the breakthrough behaviour of HOSs-25% (Fig. 6), considering the breakthrough time, the equilibrium adsorption capacity and the stability performance together, we conclude that HOSs-25% exhibits the best dynamic adsorption performance compared to commercial AC and SG.⁶⁹

With respect to the experiments performed using water-saturated carrier gas, the dynamic adsorption of n-hexane on HOSs-25% shows similar results (Fig. S12). The breakthrough time for HOSs-25% using water-saturated carrier gas is about 50 min, shorter than that without water vapor (~60 min). Longer t_c and a little higher q_{hexane} are observed, with $q_{\text{hexane}}/q_{\text{water}}$ of about 70 (Table S5). The results further confirm that the HOSs-25% has higher affinity for VOCs as compared with water vapor.

4. Conclusions

In this study, HOSs were synthesized by co-condensation of TEOS and BTSE. The resultant HOSs samples exhibit uniform mesoporous hollow spherical structures with hydrophobic organosiliceous framework. As indicated by the static adsorption-desorption results, HOSs composites have good affinity towards VOCs, low water vapor capacity and good stability. The equilibrium adsorption capacity of water vapor, n-hexane and 93# gasoline on HOSs-25% (0.0120 g g⁻¹, 1.36 g g⁻¹ and 1.35 g g⁻¹, respectively) is better than that of AC (0.604 g g⁻¹, 0.639 g g⁻¹ and 0.666 g g⁻¹, respectively) and SG (0.445 g g⁻¹, 0.438 g g⁻¹ and 0.445 g g⁻¹, respectively). The water vapor adsorption capacities of all the samples are linear to the corresponding densities of surface hydroxyl groups. HOSs-25% exhibits the best dynamic adsorption, desorption performance and stability. With excellent adsorption and desorption performance and stability, HOSs with hierarchical micro/mesoscopic structure could have a promising future in VOC emission controlling.

Acknowledgements

This work is supported by the National Science Foundations of China (21101017, 21103014 and 21201026), Jiangsu province science and technology support program (BE2011651), Key University Science Research Project of Jiangsu Province

(11KJA610002), the Opening Fund from Provincial Key Laboratory of Oil & Gas Storage and Transportation Technology, Jiangsu, P. R. China (cyl201), and sponsored by Qing Lan Project.

5

Notes and references

- ^a Jiangsu Key Laboratory of Advanced Catalytic Materials and Technology, Changzhou University, 1 Gehu Road, Changzhou, Jiangsu 213164, PR China
- ^b Australian Institute for Bioengineering and Nanotechnology, The University of Queensland, Brisbane, QLD 4072, Australia
- ^c Jiangsu Provincial Key Laboratory of Oil and Gas Storage and Transportation Technology, Changzhou University, Xingyuan 15 Road, Changzhou, Jiangsu, 213016, P. R. China
- ^d Research and Development Center, China Tobacco Anhui Industrial Co., Ltd., 9 Tianda Road, Hefei, Anhui, 230028, P. R. China
- 20 1 M. Guillemot, J. Mijoin, S. Mignard and P. Magnoux, *Ind. Eng. Chem. Res.*, 2007, **46**, 4614.
 - 2 D. P. Serrano, G. Calleja, J. A. Botas and F. J. Gutierrez, *Ind. Eng. Chem. Res.*, 2004, **43**, 7010.
 - 3 X. J. Hu, S. Z. Qiao, X. S. Zhao and G. Q. Lu, *Ind. Eng. Chem. Res.*, 2001, **40**, 862.
 - 25 4 S. D. Manjare, A. K. Ghoshal, *Ind. Eng. Chem. Res.*, 2006, **45**, 6563.
 - 5 F. Fajula, D. Plee, *Stud. Surf. Sci. Catal.*, 1994, **85**, 633.
 - 6 S. W. Blocki, *Environ. Prog.*, 1993, **12**, 226.
 - 7 A. Stein, *Adv. Mater.*, 2003, **15**, 763.
 - 30 8 Q. B. Wang, L. Yan, H. Yan, *Chem. Commun.*, 2007, 2339.
 - 9 B. L. Newalkar, N. V. Choudary, U. T. Turaga, R. P. Vijayalakshmi, P. Kumar, S. Komarneni and T. S. G. Bhat, *Chem. Mat.*, 2003, **15**, 1474.
 - 10 B. L. Newalkar, N. V. Choudary, U. T. Turaga, R. P. Vijayalakshmi, P. Kumar, S. Komarneni and T. S. G. Bhat, *Microporous and Mesoporous Mat.*, 2003, **65**, 267.
 - 35 11 W. G. Shim, J. W. Lee, H. Moon, *Sep. Sci. Technol.*, 2006, **413**, 693.
 - 12 L. Huang, Q. L. Huang, H. N. Xiao and M. Eic, *Microporous Mesoporous Mat.*, 2007, **98**, 330.
 - 40 13 P. A. Russo, M. M. L. R. Carrott, P. J. M. Carrott, *Int. Adsorpt. Soc.*, 2008, **14**, 367.
 - 14 B. Dou, Q. Hu, J. Li, S. Qiao and Z. Hao, *J. Hazard. Mater.*, 2011, **186**, 1615.
 - 15 P. A. Russo, M. Carrott, P. J. M. Carrott, *New J. Chem.*, 2011, **35**, 115
 - 45 407.
 - 16 K. Kosuge, S. Kubo, N. Kikukawa, M. Takemori, *Langmuir*, 2007, **23**, 3095.
 - 17 A. Matsumoto, H. Misran, K. Tsutsumi, *Langmuir*, 2004, **20**, 7139.
 - 18 R. Serna-Guerrero, A. Sayari, *Environ. Sci. Technol.*, 2007, **41**, 4761.
 - 50 19 A. Stein, B. J. Melde, R. C. Schroden, *Adv. Mater.*, 2000, **12**, 1403.
 - 20 F. Hoffmann, M. Cornelius, J. Morell and M. Fröba, *Angew. Chem. Int. Edit.*, 2006, **45**, 3216.
 - 21 J. M. Kistler, M. L. Gee, G. W. Stevens and A. J. O'Connor, *Chem. Mat.*, 2003, **15**, 619.
 - 55 22 S. Inagaki, S. Y. Guan, Y. Fukushima, T. Ohsuna and O. Terasaki, *J. Am. Chem. Soc.*, 1999, **121**, 9611.
 - 23 C. M. Bamnoligh, R. C. T. Slade, R. T. Williams, *J. Mater. Chem.*, 1998, **8**, 569.
 - 24 I. Batonneau-Gener, A. Yonli, A. Trouve, S. Mignard, M. Guidotti, M. Sgobba, *Sep. Sci. Technol.*, 2010, **45**, 768.
 - 60 25 F. Caruso, R. A. Caruso, H. Mohwald, *Science*, 1998, **282**, 1111.
 - 26 X. W. Lou, L. A. Archer, Z. C. Yang, *Adv. Mater.*, 2008, **20**, 3987.
 - 27 Y. Wang, A. S. Angelatos, F. Caruso, *Chem. Mat.*, 2008, **20**, 848.
 - 28 J. Liu, F. Liu, K. Gao, J. S. Wu and D. F. Xue, *J. Mater. Chem.*, 2009, **19**, 6073.
 - 29 Q. Zhang, W. S. Wang, J. Goebl and Y. D. Yin, *Nano Today*, 2009, **4**, 494.
 - 30 J. W. Tang, X. F. Zhou, D. Y. Zhao, G. Q. Lu, J. Zou, C. Z. Yu, *J. Am. Chem. Soc.*, 2007, **129**, 9044.
 - 70 31 J. Zhu, J. W. Tang, L. Z. Zhao, X. F. Zhou, Y. H. Wang and C. Z. Yu, *Small*, 2010, **6**, 276.
 - 32 J. Hu, M. Chen, X. Fang, L. Wu, *Chem. Soc. Rev.*, 2011, **40**, 5472.
 - 33 H. N. Wang, M. Tang, K. Zhang, D. F. Cai, W. Q. Huang, R. Y. Chen and C. Z. Yu, *J. Hazard. Mater.*, 2014, **268**, 115.
 - 75 34 H. Y. Zhu, X. S. Zhao, G. Q. Lu and D. D. Do, *Langmuir*, 1996, **12**, 6513.
 - 35 Y. D. Xia, G. S. Walker, D. M. Grant, R. Mokaya, *J. Am. Chem. Soc.*, 2009, **131**, 16493.
 - 36 J. X. Hu, H. Shang, J. G. Wang, L. Luo, Q. Xiao, Y. J. Zhong, W. D. Zhu, *Ind. Eng. Chem. Res.*, 2014, **53**, 11828
 - 80 37 A. J. Fletcher, E. J. Cussen, D. Bradshaw, M. J. Rosseinsky and K. M. Thomas, *J. Am. Chem. Soc.*, 2004, **126**, 9750.
 - 38 J. Sears, W. George, *Anal. Chem.*, 1956, **28**, 1981.
 - 39 Z. H. Ouyang, L. Wu, K. B. Li, S. C. Cao, Y. Wang, L. Lian, D. L. Yi and X. R. Qin, *Chem. Ind. Eng. Prog.*, 2005, **24**, 1265.
 - 85 40 S. Z. Qiao, C. X. Lin, Y. G. Jin, Z. Li, Z. M. Yan, Z. P. Hao, Y. N. Huang and G. Q. Lu, *J. Phys. Chem. C*, 2009, **113**, 8673.
 - 41 G. E. Fryxell, S. V. Mattigod, Y. Lin, H. Wu, S. Fiskum, K. Parker, F. Zheng, W. Yantasee, T. S. Zemanian and R. S. Adleman, *J. Mater. Chem.*, 2007, **17**, 2863.
 - 90 42 Q. S. Huo, J. Liu, L. Q. Wang, Y. B. Jiang, T. N. Lambert, E. Fang, *J. Am. Chem. Soc.*, 2006, **128**, 6447-6453.
 - 43 K. Suzuki, K. Ikari, H. Imai, *J. Am. Chem. Soc.*, 2004, **126**, 462-463.
 - 44 Q. H. Yang, J. Yang, J. Liu, Y. Li and C. Li, *Chem. Mater.*, 2005, **17**, 3019.
 - 95 45 Y. Oaki, A. Kotachi, T. Miura and H. Imai, *Adv. Funct. Mater.*, 2006, **16**, 1633.
 - 46 J. Liu, Q. Yang, L. Zhang, D. Jiang, X. Shi, J. Yang, H. Zhong and C. Li, *Adv. Funct. Mater.*, 2007, **17**, 569-576.
 - 100 47 L. Zhang, J. Liu, J. Yang, Q. H. Yang and C. Li, *Microporous Mesoporous Mat.*, 2008, **109**, 172.
 - 48 T. W. Kim, F. Kleitz, B. Paul, R. Ryoo, *J. Am. Chem. Soc.*, 2005, **127**, 7601.
 - 49 R. Richer, L. Mercier, *Chem. Mater.*, 2001, **13**, 2999.
 - 50 M. A. Wahab, Kim, II, C. S. Ha, *Microporous Mesoporous Mater.*, 2004, **69**, 19.
 - 51 J. P. Gallas, J. M. Goupil, A. Vimont, J. C. Lavalley, B. Gil, J. P. Gilson and O. Miserque, *Langmuir*, 2009, **25**, 5825.
 - 52 Y. Bai, Z. H. Huang, F. Y. Kang, *J. Mater. Chem. A*, 2013, **1**, 9536.
 - 110 53 Y. Bai, Z. H. Huang, F. Y. Kong, *Carbon*, 2014, **66**, 705.
 - 54 M. C. Capel-Sanchez, L. Barrio, J. M. Campos-Martin, J. L. G. Fierro, *J. Colloid Interface Sci.*, 2004, **277**, 146.
 - 55 U. Cvelbar, M. Mozetic, I. Junkar, A. Vesel, J. Kovac, A. Drenik, T. Vrlinic, N. Hauptman, M. Klanjssek-Gunde, B. Markoli, N. Krstujovic, S. Milosevic, F. Gaboriau, T. Belmonte, *Appl. Surf. Sci.*, 2007, **253**, 8669.
 - 56 G. Marban, A. B. Fuertes, *Carbon*, 2004, **42**, 71.
 - 57 F. Cosnier, A. Celzard, G. Furdin, D. Begin and J. F. Mareche, *Adsorpt. Sci. Technol.*, 2006, **24**, 215.
 - 120 58 D. Kaplan, I. Nir, L. Shmueli, *Carbon*, 2006, **44**, 3247.
 - 59 N. Qi, W. S. Appel, M. D. LeVan and J. E. Finn, *Ind. Eng. Chem. Res.*, 2006, **45**, 2303.
 - 60 J. Mollmer, M. Lange, A. Moller, C. Patzschke, K. Stein, D. Lassig, J. Lincke, R. Glaser, H. Krautscheid, R. Staudt, *J. Mater. Chem.*, 2012, **22**, 10274.
 - 125 61 J. Moellmer, A. Moeller, F. Dreisbach, R. Glaeser, R. Staudt, *Microporous Mesoporous Mat.*, 2011, **138**, 140-148.
 - 62 M. V. Parkes, C. L. Staiger, J. J. Perry, M. D. Allendorf, J. A. Greathouse, *Phys. Chem. Chem. Phys.*, 2013, **15**, 9093.
 - 130 63 Z. J. Zhang, S. K. Xian, Q. B. Xia, H. H. Wang, Z. Li, J. Li, Aiche J., 2013, **59**, 2195.
 - 64 A. S. Gonzalez, M. G. Plaza, F. Rubiera, C. Pevida, *Chem. Eng. J.*, 2013, **230**, 456.
 - 65 A. Mouahid, D. Bessieres, F. Plantier, G. Pijaudier-Cabot, *J. Therm. Anal. Calorim.*, 2012, **109**, 473.
 - 135 66 I. Esteves, M. S. S. Lopes, P. M. C. Nunes, J. P. B. Mota, *Sep. Purif.*

-
- Technol.*, 2008, **62**, 281.
- 67 F. Lu, S. H. Wu, Y. Hung, C. Y. Mou, *Small*, 2009, **5**, 1408-1413.
- 68 K. Hiro, S. Renichirou, Foundation and Design of Adsorptions. *Chemical Industry Press*: Beijing, 1983.
- 5 69. B. Cardoso, A. S. Mestre, A. P. Carvalho, J. Pires, *Ind. Eng. Chem. Res.*, 2008, **47**, 5841.